Article | Open Access

Micro Nano Science

Pan *et al. Micro Nano Sci.* **2026**, *1*, 7 **DOI:**10.20517/mns.2025.08

Thermal-direction-controlled architecture in magnetic polymer/carbon microspheres

Panpan Pan[1,3], Xianjiao Shao[1], Dongsheng Ma[2], Yuanhao Xing[1], Xiaowei Cheng[3], Minjie Wang[4], Liwei Mi[4,*], Qin Yue[2,*]

Keywords:
Core-shell, yolk-shell, mesoporous polymer/carbon, heat-transfer direction, magnetic materials

Citation: Pan, P.; Shao, X.; Ma, D.; Xing, Y.; Cheng, X.; Wang, M.; Mi, L.; Yue, Q. Thermal-direction-controlled architecture in magnetic polymer/carbon microspheres. *Micro Nano Sci.* **2026**, *1*, 7. https://dx.doi.org/10.20517/mns.2025.08

Received: 25 Nov 2025 **First Decision:** 19 Dec 2025 **Revised:** 10 Feb 2026 **Accepted:** 16 Mar 2026 **Published:** 23 Apr 2026

Academic Editor: Lu Han
Copy Editor: Shu-Yuan Duan
Production Editor: Shu-Yuan Duan

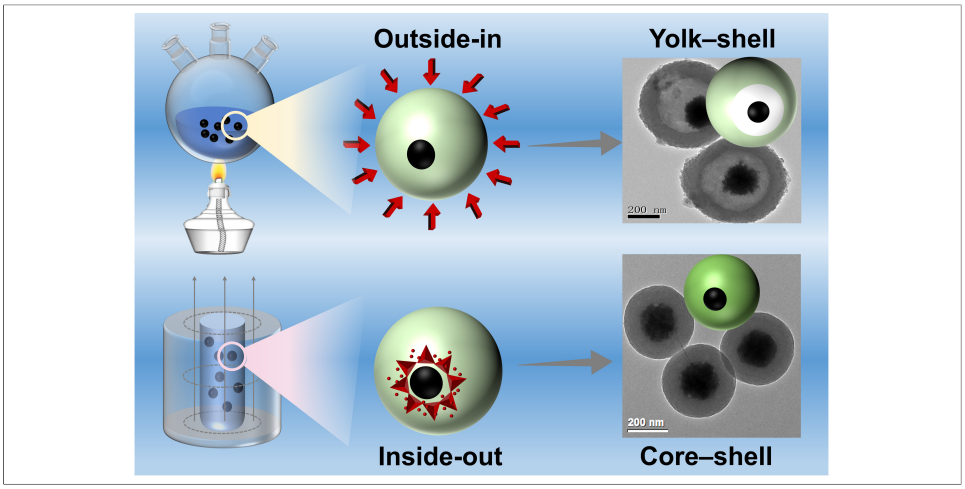

Abstract

The precise control over the architecture of magnetic core-shell microspheres is crucial for advanced applications. While synthetic methods are well-established, the influence of heat-transfer direction during polymer curing on the final carbon structure remains unexplored. Herein, monodisperse Fe_3O_4@resorcinol-formaldehyde core-shell microspheres were synthesized as a model platform to investigate this principle. We consistently show that the thermal pathway governs the morphological evolution during carbonization, as supported by time-resolved electron microscopy: conventional external heating (outside-in) yields yolk-shell structures, whereas magnetically inductive heating (inside-out) produces solid core-shell configurations. Time-resolved electron microscopy reveals that this distinct structural divergence stems from gradient-induced shell shrinkage. This thermal-direction control was extended to other substrates, highlighting its generality. Furthermore, the resulting nitrogen-doped Fe_3O_4@C-N microspheres serve as

[1]Marine College, Shandong University, Weihai 264209, Shandong, China.
[2]Institute of Fundamental and Frontier Sciences, University of Electronic Science and Technology of China, Chengdu 610054, Sichuan, China.
[3]Department of Chemistry, Department of Gastroenterology, Zhongshan Hospital of Fudan University, Shanghai Key Laboratory of Molecular Catalysis and Innovative Materials, State Key Laboratory of Molecular Engineering of Polymers, Fudan University, Shanghai 200433, China.
[4]School of Chemistry and Environmental Engineering, Yaoshan laboratory, Pingdingshan University, Pingdingshan 467000, Henan, China.

[*]**Correspondence to:** Prof. Qin Yue, Institute of Fundamental and Frontier Sciences, University of Electronic Science and Technology of China, Chengdu 610054, Sichuan, China. E-mail: qinyue@uestc.edu.cn; Prof. Liwei Mi, School of Chemistry and Environmental Engineering, Yaoshan laboratory, Pingdingshan University, Pingdingshan 467000, Henan, China. E-mail: mlwzzu@163.com

efficient magnetically recoverable solid-base catalysts, achieving near-quantitative conversion (99.78%) and yield (98.57%) in biodiesel production from corn oil. This work establishes heat-flow manipulation as a versatile strategy for tailoring carbon architectures and provides insights for designing functional catalytic materials.

INTRODUCTION

Magnetic polymer/carbon microspheres with tunable core-shell and yolk-shell configurations are highly attractive for applications in catalysis, adsorption, energy storage, and photonic materials, as their architecture governs mass/charge transport, interfacial properties, and mechanical stability[1-3]. Sol-gel methods, particularly Stöber-like interfacial assembly, offer a robust and versatile route to fabricate uniform shells on magnetic cores under mild conditions[4-7]. For instance, silica shells with controllable thickness can be readily deposited onto Fe_3O_4 nanoparticles via base-catalyzed hydrolysis and condensation of alkoxysilanes [e.g., tetraethyl orthosilicate (TEOS)] in alcohol-water mixtures[8-11]. Similarly, metal oxide shells such as titania have been coated onto magnetic cores using analogous Stöber-like processes[12-15].

Beyond inorganic coatings, resorcinol-formaldehyde (RF) resin synthesized via sol-gel polymerization serves as a standard precursor for polymer-derived carbon shells and supports[16-17]. RF resins, formed through step-growth polymerization, exhibit high thermal stability and have been extensively used to produce carbon gels, catalyst supports, adsorbents, mesoporous carbons, and electrode materials[18-29]. Various polymer shells [e.g., polystyrene (PS), polymethyl methacrylate (PMMA), polyaniline (PANI), phenol-formaldehyde resin (PF), RF] have been incorporated onto magnetic particles via methods such as hydrothermal PF coating using phenol and hexamethylenetetramine (HMT) and microwave-assisted RF coating on Fe_3O_4[30-41]. Despite the availability of numerous polymer-condensation strategies, facile interfacial approaches that yield monodisperse core-shell polymer particles suitable for assembling photonic crystals remain limited[42-45]. Moreover, the cross-linking degree of the polymer shell critically influences its structural integrity during thermal treatment[47-49]. Conventional annealing, typically involving external heating, transfers heat from the outside inward, but the effect of reversed heat flux (inside-out) on structural evolution remains unexplored[49-54]. A systematic comparison of curing pathways is essential to understand the polymerization-structure relationship and achieve precise architectural control[55-59].

This work aims to elucidate the correlation between heat transfer direction during curing and the structural evolution of carbon shells in magnetic core-shell microspheres, and to develop a viable thermal regulation strategy for precisely controlling carbon-based microstructures. Monodisperse Fe_3O_4@RF core-shell microspheres with tunable shell thickness were synthesized via interfacial sol-gel polymerization using Fe_3O_4 nanoparticles as cores and RF resin as the shell. These microspheres served as a model system for subsequent investigations. By designing distinct curing pathways with different heat transfer directions, we examined the influence of heat flow on carbon shell development. Time-resolved scanning electron microscopy (SEM) and transmission electron microscopy (TEM) analyses were employed to uncover the intrinsic relationship between curing routes and morphological evolution, leading to a proposed structural transformation mechanism. Furthermore, the RF-coating strategy was extended to other nanomaterial substrates to evaluate its universality. Nitrogen-doped magnetic carbon microspheres, obtained through ammonia treatment, were further explored for their catalytic functionality. This study offers a new thermal processing strategy for tailoring carbon-based microsphere architectures for advanced catalytic applications.

EXPERIMENTAL

Chemicals

Resorcinol, formaldehyde, ammonium hydroxide, $FeCl_3 \cdot 6H_2O$, trisodium citrate, sodium hydroxide, ethylene glycol, sodium acetate, carbon nanotubes (CNTs), corn oil, and ethanol were of analytical grade and purchased from Shanghai Chemical Corp. Deionized water was used for all experiments.

Synthesis of the magnetic nanoparticles (Fe_3O_4 NPs)

Hydrophilic Fe_3O_4 nanoparticles were synthesized following a previously reported method[60]. In a typical procedure, $FeCl_3 \cdot 6H_2O$ (3.25 g), trisodium citrate (1.3 g), and sodium acetate (6.0 g) were dissolved in ethylene glycol (100 mL) under magnetic stirring at 600 rpm and room temperature (25 °C) for 30 min. The resulting yellow solution was transferred into a 200 mL Teflon-lined stainless-steel autoclave, which was sealed and heated at 200 °C for 10 h. After cooling to room temperature naturally, the black product was collected and washed three times each with deionized water and ethanol.

Synthesis of core-shell Fe_3O_4@RF/C and yolk-shell Fe_3O_4@C microspheres

The RF shell was coated via a base-catalyzed sol-gel process in a mixed ethanol/water system. Typically, 100 mg of the synthesized magnetic nanoparticles were dispersed in a mixture of ethanol (20 mL) and water (10 mL). Then, 1.0 mL of ammonium hydroxide solution was added, and the resulting mixture was stirred magnetically at 500 rpm for 2 h at room temperature (25 °C). The resulting Fe_3O_4@RF microspheres were magnetically separated and washed three times alternately with deionized water and ethanol. To obtain yolk-shell Fe_3O_{4Su}@C microspheres, the reaction solution was further subjected to external pre-curing at 100 °C for varying durations before being calcined in a tube furnace at 600 °C for 5 h under nitrogen. The pre-curing step at 100 °C establishes a controlled and reproducible bulk-heating environment that accelerates the polycondensation of RF resin, enabling systematic modulation of the curing degree over time while maintaining a constant external temperature.

Synthesis of CNT@RF and Ag@RF

The procedure is the same as above, except that CNTs (or Ag) are used instead of magnetic nanoparticles.

Alternating magnetic field curing of Fe_3O_4@RF

To achieve heating of the microspheres from the inside out, the characteristic of rapid heat generation due to the accelerated motion between particles in an alternating magnetic field (AMF) was utilized. The magnetic nuclei were used as the heat source to cure the microspheres. Specifically, the Fe_3O_4@RF microspheres, after reacting at room temperature, along with the reaction solution, were placed in an AMF and heated for 10 min. The temperature in the reaction solution gradually increased to 67 °C and remained stable. Because the local temperature at the Fe_3O_4 core/shell interface cannot be directly measured in our setup, magnetically inductive heating (MIH) is described here in terms of core-localized heating under an AMF rather than a quantified radial temperature profile. The microspheres were then separated using a magnet, washed three times each with ethanol and water, vacuum-dried at 40 °C, and calcined in nitrogen at 600 °C for 5 h before use. In this study, MIH is used operationally to deliver core-localized heating to Fe_3O_4@RF precursors. The bulk solution temperature was monitored with a thermocouple and reached 67 °C after 10 min of AMF exposure.

Ammonia treatment of Fe_3O_4@C microspheres

Nitrogen doping of Fe_3O_4@C microspheres was achieved by ammonia treatment in a tube furnace. The temperature was gradually increased to 600 °C in nitrogen at a rate of 2 °C/min, then maintained at 600 °C for 5 h in an NH_3/Ar mixture (1:9), followed by cooling in nitrogen. The samples were removed and washed with deionized water until the pH of the supernatant was neutral. They were then vacuum dried at 40°C for later use, and the samples were designated Fe_3O_4@C-N.

Catalytic transesterification reaction

The Fe_3O_4@C-N microspheres were employed as a magnetically recoverable solid-base catalyst for heterogeneous catalysis. In this study, the transesterification of corn oil with methanol was selected as a model reaction for biodiesel production. The reaction was conducted in a 100 mL magnetically stirred

autoclave. Typically, corn oil and methanol were mixed at a molar ratio of 1:100, followed by the addition of Fe_3O_4@C-N microspheres (10 wt.% relative to the weight of corn oil). The mixture was maintained at 180 °C for 6 h under continuous magnetic stirring at 800 rpm. After completion, the products were separated, and the biodiesel content was quantitatively analyzed using a high-performance liquid chromatography with UV detection (HPLC-UV) system.

Measurement and characterization

TEM was performed using a JEOL 2011 microscope (JEOL Ltd., Japan) operated at 200 kV. Samples were dispersed in ethanol (or deionized water), drop-cast onto carbon-film-coated copper grids, and dried prior to analysis. The surface morphology of the microspheres was examined by SEM (Nova NanoSEM 450, FEI, USA) at an accelerating voltage of 20 kV. Powder X-ray diffraction (XRD) patterns were recorded on a Bruker D4 X-ray diffractometer (Bruker, Germany) using Ni-filtered Cu Kα radiation (40 kV, 40 mA). X-ray photoelectron spectroscopy (XPS) measurements were conducted on a Thermo Scientific K-Alpha spectrometer (Thermo Fisher Scientific, USA) at room temperature using a Mg Kα X-ray source. HPLC-UV was carried out on an LC-20AT system (Shimadzu, Japan).

RESULTS AND DISCUSSION

Monodisperse spherical Fe_3O_4@RF core-shell precursors with tunable shell thickness (~ 400 nm in total diameter) were synthesized and self-assembled into photonic arrays [Figure 1A]. Following calcination at 600 °C under N_2, the derived Fe_3O_4@C particles maintained uniform spherical morphology and excellent dispersibility [Figure 1B]. TEM analysis revealed that the Fe_3O_4@RF precursors possess a well-defined core-shell structure, comprising a compact Fe_3O_4 core (~ 120 nm in diameter) and a lower-density RF shell (~ 125 nm thick) [Figure 1C]. After carbonization, the spherical architecture was preserved in the resulting Fe_3O_4@C product [Figure 1D]. This structural retention indicates that the RF oligomers underwent further polymerization, condensation, and framework shrinkage during thermal treatment. These well-defined precursor particles provide a controlled platform to investigate how the direction of heat transfer during curing and carbonization dictates the final structural characteristics.

The thickness of the RF/carbon shell is primarily governed by the concentration of the RF resin, demonstrating that the shell thickness can be precisely controlled by tuning the synthesis parameters. Fe_3O_4@RF microspheres with varying RF shell thicknesses (~ 7, 15, 75, 150 nm) were successfully synthesized by adjusting the resorcinol concentration (~ 1, 2, 3, 5 mg/mL), respectively [Figure 2]. After calcination at 600 °C under N_2, the resulting carbon shell thickness scales linearly with that of the precursor RF shell. For example, an MIH-cured Fe_3O_4@RF particle with an ~ 110 nm RF shell yields an Fe_3O_4@C particle with an ~ 82 nm carbon shell, confirming that the final shell dimension is predominantly defined during the polymeric precursor stage. The XRD pattern of Fe_3O_4@C [Figure 3] shows the characteristic broad peak of amorphous carbon. Furthermore, the diffraction peaks corresponding to the face-centered cubic (fcc) Fe_3O_4 phase (JCPDS No. 19-0629) remain intact, confirming the thermal stability of the Fe_3O_4 core throughout the high-temperature calcination process.

To investigate outside-in curing, Fe_3O_4@RF precursors were externally pre-cured at 100 °C for varying durations prior to carbonization under nitrogen [Figure 4]. This temperature was chosen to provide stable, uniform external heating, enabling time-dependent control over RF curing at a fixed bulk temperature. After prepolymerizing RF resin on the Fe_3O_4 nanoparticles at room temperature for 4 h, the reaction vessel was immersed in a 100 °C oil bath. SEM and TEM images confirm that all samples, pre-cured from 5 min to 8 h at 100 °C, retained well-dispersed spherical morphology. A short pre-curing time (~ 5 min) establishes a pronounced surface-to-center curing gradient during carbonization, causing the less-condensed inner RF to

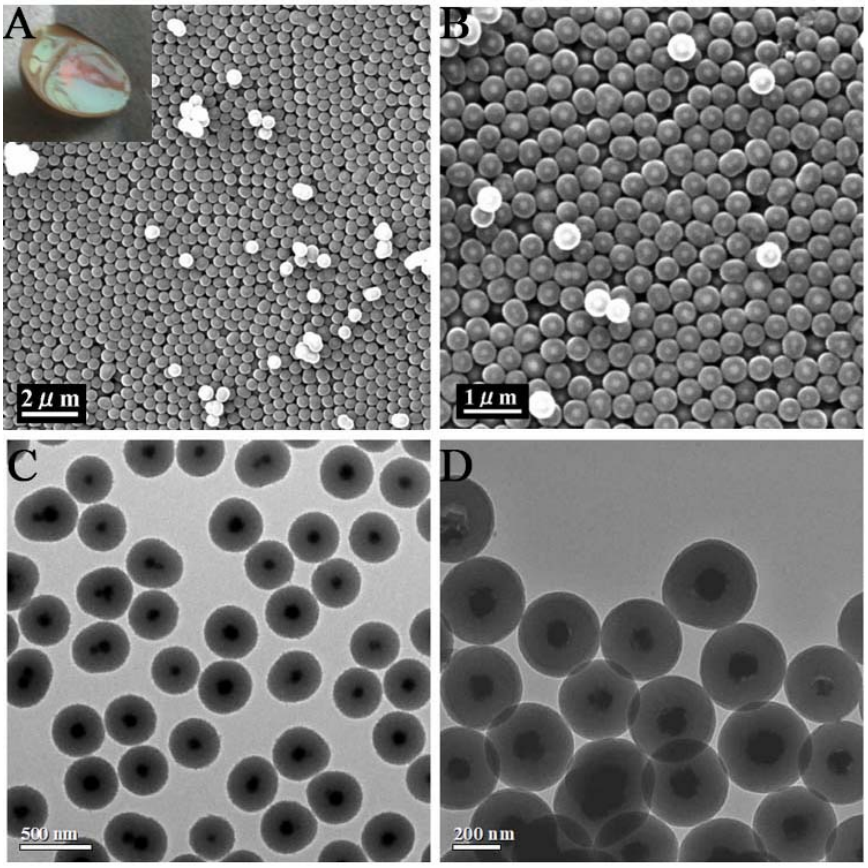

Figure 1. Structure characterizations of Fe_3O_4@RF and Fe_3O_4@C microspheres. (A) SEM image of Fe_3O_4@RF; the inset shows their optical photograph; (B) SEM image of Fe_3O_4@C; (C) TEM image of Fe_3O_4@RF; (D) TEM image of Fe_3O_4@C. RF: Resorcinol-formaldehyde; SEM: scanning electron microscopy; TEM: transmission electron microscopy.

shrink more than the crosslinked outer layer [Figure 4A and B], yielding yolk-shell Fe_3O_4@C particles with a low-density carbon shell (~ 110 nm thick) and a large interior cavity (~ 400 nm in diameter). Fractured microspheres clearly reveal the presence of the cavity and the core. Extending pre-curing to 1 h [Figure 4C and D] and 2.5 h [Figure 4E and F] progressively thickens the load-bearing crosslinked region, reducing the cavity diameter from ~ 340 nm to ~ 310 nm while increasing the carbon shell thickness from ~ 130 nm to ~ 175 nm. After 8 h of pre-curing, the cavities disappear completely, resulting in solid core-shell Fe_3O_4@C microspheres [Figure 4G and H]. Morphological metrics including shell thickness, cavity size, and shrinkage percentage were quantified by statistical analysis of TEM images [mean ± standard deviation (SD), $n \geq 50$] as summarized in Supplementary Figure 1A-C, confirming the reproducibility of this structural evolution.

Based on the observed structural evolution, a mechanism for the formation of rattle-like Fe_3O_4@C microspheres through an outside-in curing gradient is proposed, as illustrated in Scheme 1. Initially, positively charged ammonium ions are electrostatically adsorbed onto the surface of negatively charged citric acid-modified Fe_3O_4 nanoparticles. Subsequently, the added resorcinol adsorbs onto the nanoparticle surface via electrostatic interaction between its negatively charged phenolic hydroxyl groups and the adsorbed ammonium ions. Upon addition of formaldehyde, the surface-adsorbed resorcinol polymerizes with formaldehyde under ammonia catalysis at room temperature, forming core-shell microspheres with Fe_3O_4 as the core and an RF oligomer shell. When the temperature is raised to 100 °C using an external heating method, further polymerization and crosslinking of the RF shell proceed in an outside-in manner. The duration of heating is identified as the key factor governing the non-uniform distribution of curing degree

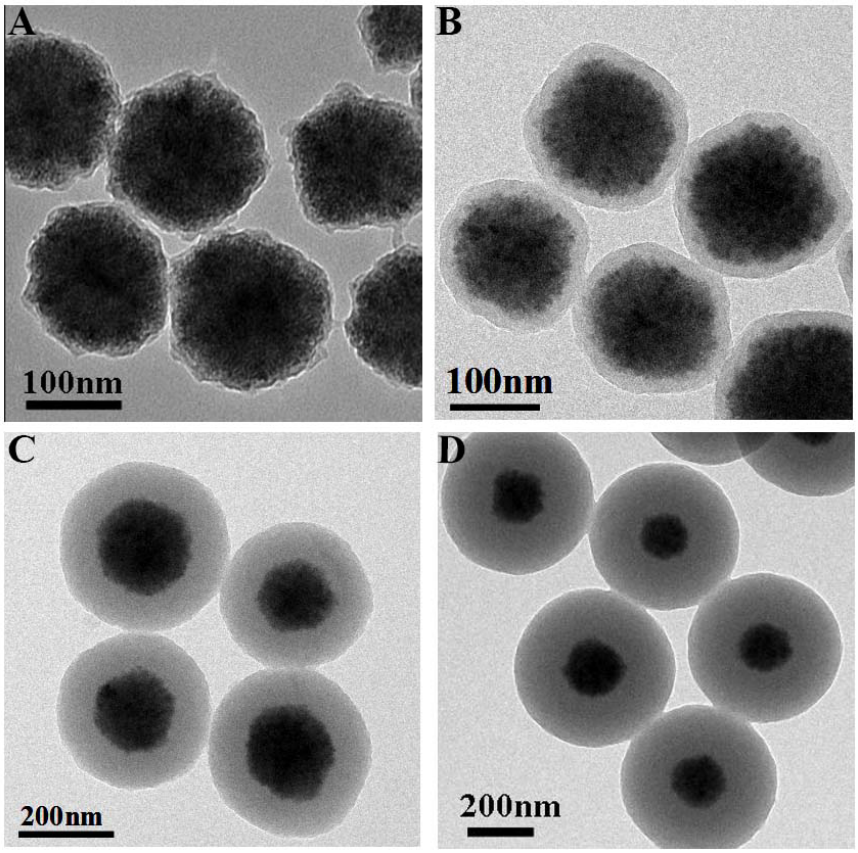

Figure 2. TEM images of Fe_3O_4@RF with RF shell thickness obtained at different reaction concentrations of resorcinol. (A) 7 nm (in 1 mg/mL); (B) 15 nm (in 2 mg/mL); (C) 75 nm (in 3 mg/mL); (D) 150 nm (in 5 mg/mL). TEM: Transmission electron microscopy; RF: resorcinol-formaldehyde.

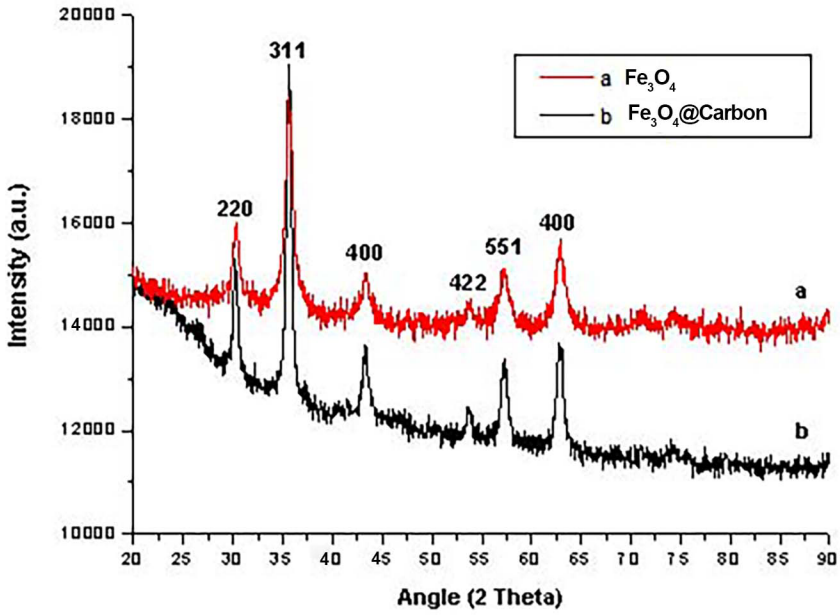

Figure 3. XRD patterns of Fe_3O_4 nanoparticles and Fe_3O_4@C microspheres. The Fe_3O_4 reflections match the cubic spinel Fe_3O_4 phase (JCPDS 19-629), and the broad feature centered at ~ 20-30° is assigned to amorphous carbon in Fe_3O_4@C. XRD: X-ray diffraction.

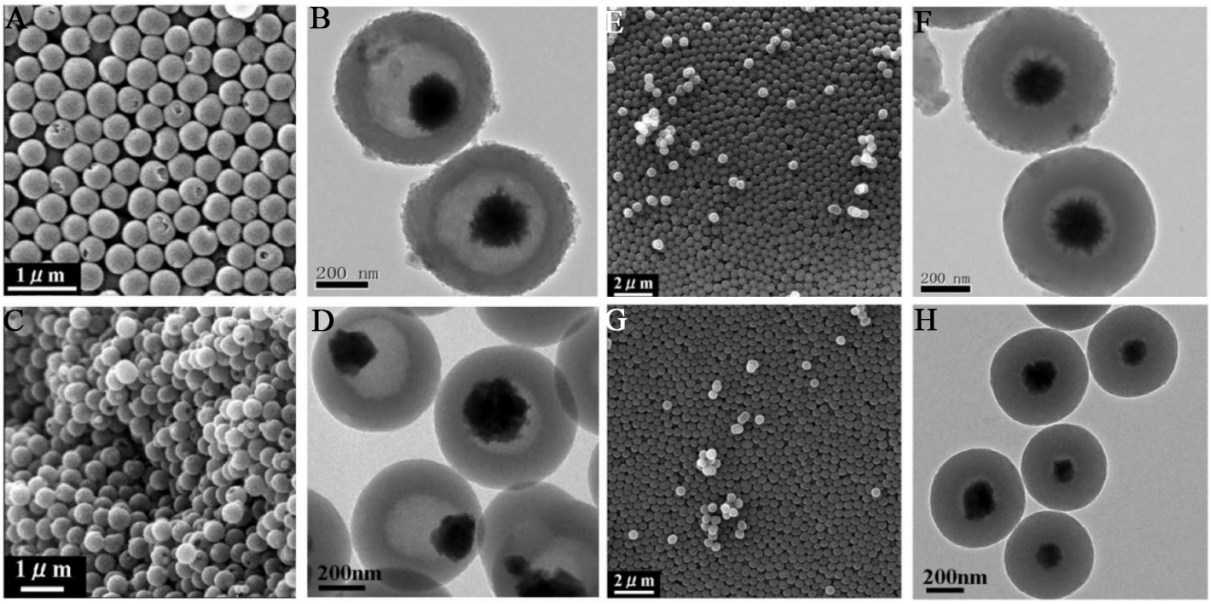

Figure 4. Morphology evolution of Fe_3O_4@C microspheres obtained with external pre-curing at 100 °C before calcination under nitrogen. (A and B) SEM and TEM images after 5 min of pre-curing; (C and D) SEM and TEM images after 1 h of pre-curing; (E and F) SEM and TEM images after 2.5 h of pre-curing; (G and H) SEM and TEM images after 8 h of pre-curing; (B, D, F and H) TEM images illustrating the structural evolution from yolk-shell to solid core-shell configurations with increasing pre-curing time. SEM: Scanning electron microscopy; TEM: transmission electron microscopy.

within the RF shell. As a result, the polymerization and condensation degree of the RF shell increases progressively from the inside outward, leading to inward-to-outward shrinkage of the shell framework during high-temperature carbonization and ultimately yielding rattle-like Fe_3O_4@C microspheres. If the heating time is too short, only the outer region of the RF shell becomes well-polymerized and condensed, producing rattle-like structures with large internal cavities. As demonstrated in Figure 4, both cavity size and carbon shell thickness can be precisely controlled by adjusting the curing time. When curing is extended to 8 h, the entire RF shell attains a high and uniform degree of crosslinking, resulting in homogeneous shrinkage during carbonization, similar to uncured Fe_3O_4@RF oligomer precursors, and yielding solid core-shell Fe_3O_4@C microspheres [Figure 4G and H]. Thus, the differential shrinkage of the RF shell framework, driven by the gradient in curing degree, is the determining factor in the formation of rattle-like Fe_3O_4@C nanostructures.

A mixture of ethanol and water is essential for synthesizing well-dispersed, uniform core-shell Fe_3O_4@RF microspheres via the interfacial polymerization sol-gel method. To verify this, control reactions were conducted in pure ethanol and pure water (in the absence of Fe_3O_4 nanoparticles). As shown in Supplementary Figure 2, homogeneous RF emulsions form only in the ethanol-water mixture, while pure water yields a transparent solution (no nanoparticles) and pure ethanol results in aggregated RF particles. This confirms that an alcohol-water mixture is critical for forming RF nanoparticles in the sol-gel process, analogous to the role of mixed solvents in the Stöber synthesis of silica spheres. Supplementary Figure 3 further compares the morphology of Fe_3O_4@RF products prepared in the ethanol-water mixture versus pure ethanol, clearly demonstrating that only aggregated structures are obtained in pure ethanol. Thus, the ethanol-water solvent system is necessary to achieve well-dispersed, uniform core-shell Fe_3O_4@RF microspheres.

Magnetic-induction heating (MIH) was employed to achieve inside-out curing by utilizing Fe_3O_4 magnetic cores as internal heat sources. Fe_3O_4@RF microspheres, synthesized at room temperature, were exposed to an AMF for 20 min [Figure 5]. This treatment produced a well-defined core-shell structure with an RF shell

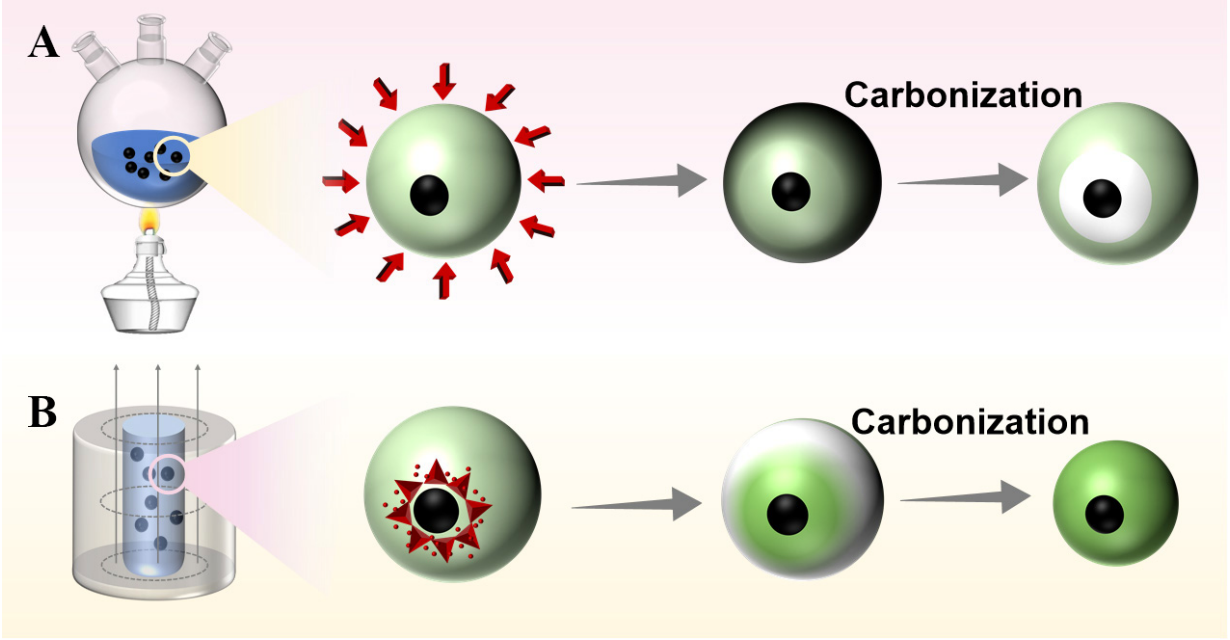

Scheme 1. (A) Formation mechanism of rattle-like Fe_3O_4@C heated in an ethanol-water mixed solvent; (B) Formation mechanism of core-shell Fe_3O_4@C heated with alternating magnetic field.

thickness of 110 nm [Figure 5A and C]. After subsequent calcination under nitrogen, the resulting magnetic carbon microspheres retained a solid core-shell morphology without intermediate cavities, and the carbon shell thickness decreased to 82 nm [Figure 5B and D], indicating that the RF shell underwent uniform contraction from the outside inward. Under AMF, the rapid oscillation of magnetic particles generates localized heat at the Fe_3O_4 core, while the polymer shell and surrounding solvent remain unaffected by the field. As illustrated in Scheme 1B, energy is deposited directly at the magnetic core, leading to a measured bulk temperature of only 67 °C after 10 min of exposure. Although the local core temperature was not directly measured, the term "inside-out" here refers specifically to energy localization at the magnetic core under AMF, with the bulk solution reaching 67 °C after 10 min. Under identical carbonization conditions, MIH-cured precursors yield solid core-shell Fe_3O_4@C particles without cavities [Figure 5B and D]. This result is consistent with preferential curing near the core-shell interface during MIH, leading to more uniform shrinkage during carbonization, a working hypothesis supported by the observed morphology.

To verify the universal applicability of the interfacial polymerization sol-gel method for coating RF polymer shells, CNTs and silver microspheres (Ag NPs) were selected as alternative core materials under otherwise identical synthesis conditions. Figure 6 presents SEM [Figure 6A and B] and TEM [Figure 6C-F] images of pristine CNTs [Figure 6A], CNT@RF [Figure 6B-D], and Ag@RF [Figure 6E and F]. After RF coating, CNT@RF hybrids remain well-dispersed and exhibit significantly increased diameters compared to bare CNTs [Figure 6A and B]. By adjusting the resorcinol concentration (~ 1 and ~ 2 mg/mL), core-shell CNT@RF structures with tunable RF shell thicknesses of approximately 33 nm and 16 nm were obtained, as shown in Figure 6A and B, respectively. TEM images of Ag@RF [Figure 6E and F] reveal uniform, well-dispersed spherical core-shell particles with an RF shell thickness of about 77 nm. These results demonstrate that the interfacial polymerization sol-gel RF coating method can be successfully extended to other nanomaterials. Moreover, this high-molecular interfacial polymerization sol-gel strategy offers a versatile platform for synthesizing diverse polymer-based nanocomposites with tailored structures and compositions

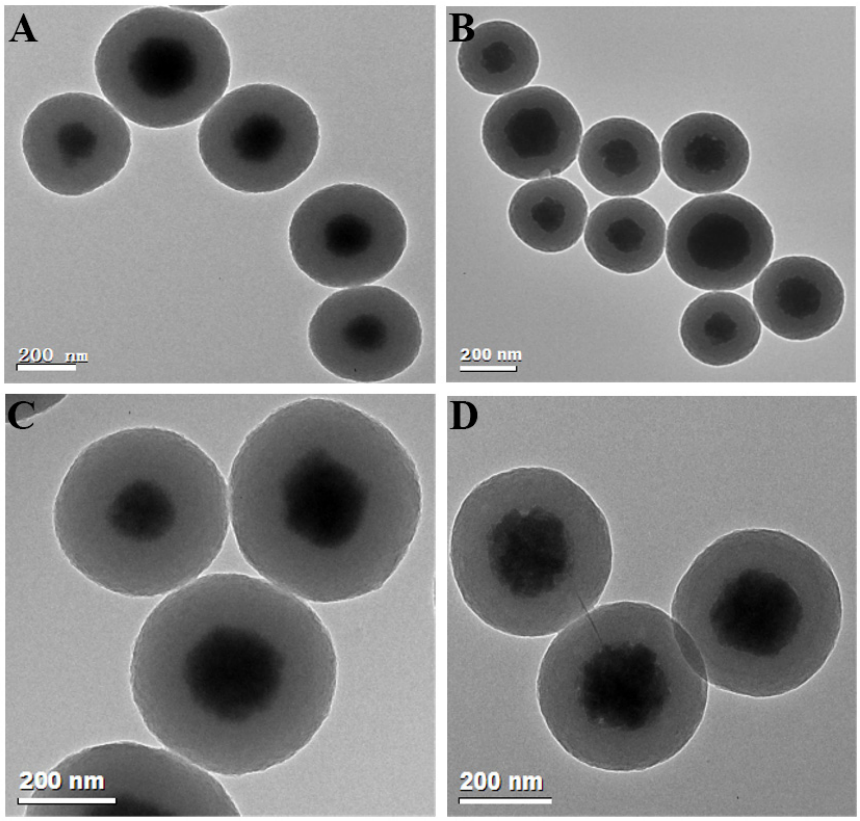

Figure 5. Morphology evolution of Fe_3O_4@RF and Fe_3O_4@C microspheres under MIH. (A) TEM image of an Fe_3O_4@RF microsphere after MIH curing; (B) TEM image of an Fe_3O_4@C microsphere obtained after calcination of the MIH-cured precursor under nitrogen; (C) High-magnification TEM image of the Fe_3O_4@RF microsphere (MIH-cured) showing the core-shell interface; (D) High-magnification TEM image of the resulting Fe_3O_4@C microsphere confirming the solid core-shell structure. RF: Resorcinol-formaldehyde; MIH: magnetically inductive heating; TEM: transmission electron microscopy.

Nitrogen-doped microspheres (denoted as Fe_3O_4@C-N) were obtained by calcining Fe_3O_4@C in ammonia at 550 °C for 3 h. XPS analysis [Figure 7] confirmed a surface N/C atomic ratio of 0.015, with four distinct nitrogen species identified: pyridinic N (398.3 eV), pyrrolic N (400.0 eV), graphitic N (401.3 eV), and oxidized N (403.1 eV). When employed as a magnetically separable solid-base catalyst for the transesterification of corn oil with methanol under optimized conditions (oil/methanol = 1:100, catalyst 10 wt.%, 180 °C, 6 h), the material achieved 99.78% conversion and a 98.57% yield of fatty acid methyl esters. The N 1s spectral deconvolution [Figure 7] reveals the presence of pyridinic, pyrrolic, and graphitic nitrogen species, which are consistent with a basic carbon shell hosting the active catalytic sites. Although described as a solid catalyst, Fe_3O_4@C-N possesses a mesoporous shell structure. N_2 sorption isotherms for Fe_3O_4@C and Fe_3O_4@C-0.1 wt.% pluronic F127 (F127) [Supplementary Figure 4] and the corresponding textural parameters [Supplementary Table 1] confirm accessible porosity that enables reagent diffusion to these basic nitrogen sites, while the Fe_3O_4 core provides magnetic recoverability. These data serve as proof-of-concept, demonstrating the catalytic accessibility of nitrogen-functionalized active sites within the porous carbon shell.

CONCLUSIONS

In this work, we aimed to elucidate how the direction of heat transfer during polymer curing governs the structural evolution of magnetic core-shell precursors. Using Fe_3O_4@RF as a model system, we decoupled the effects of thermal pathways from those of shell thickness and demonstrated that external heating from the outside in generates a curing gradient, resulting in differential shrinkage and the formation of yolk-shell

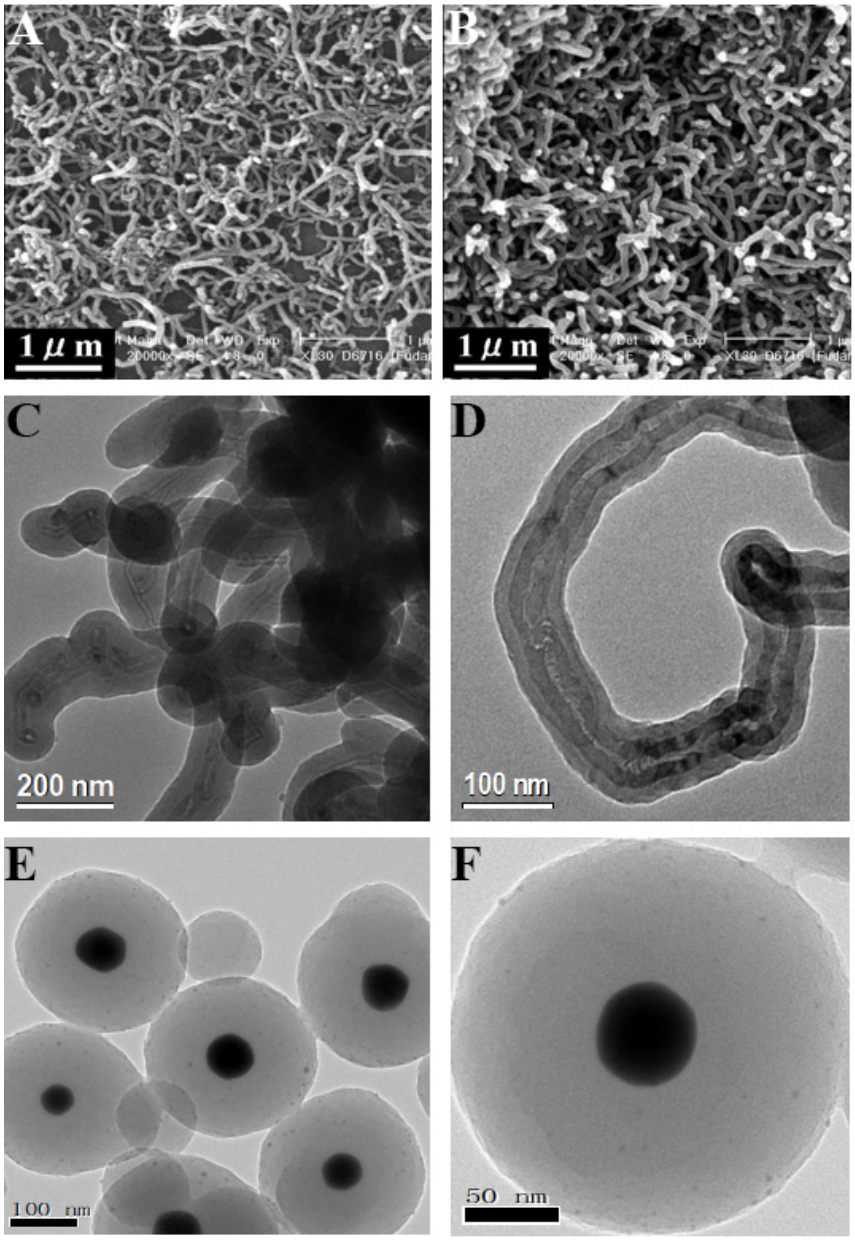

Figure 6. SEM and TEM images of CNT, CNT@RF, and Ag@RF nanostructures. (A) SEM image of CNTs; (B-D) SEM and TEM images of CNT@RF; (E and F) TEM images of Ag@RF. SEM: Scanning electron microscopy; TEM: transmission electron microscopy; CNT: carbon nanotube; RF: resorcinol-formaldehyde.

Fe_3O_4@C structures upon carbonization. Conversely, inside-out magnetic induction heating promotes uniform curing and yields solid core-shell Fe_3O_4@C under identical carbonization conditions. These findings establish thermal-direction control as a general and practical strategy for engineering carbon architectures with tailored structures for advanced functional applications.

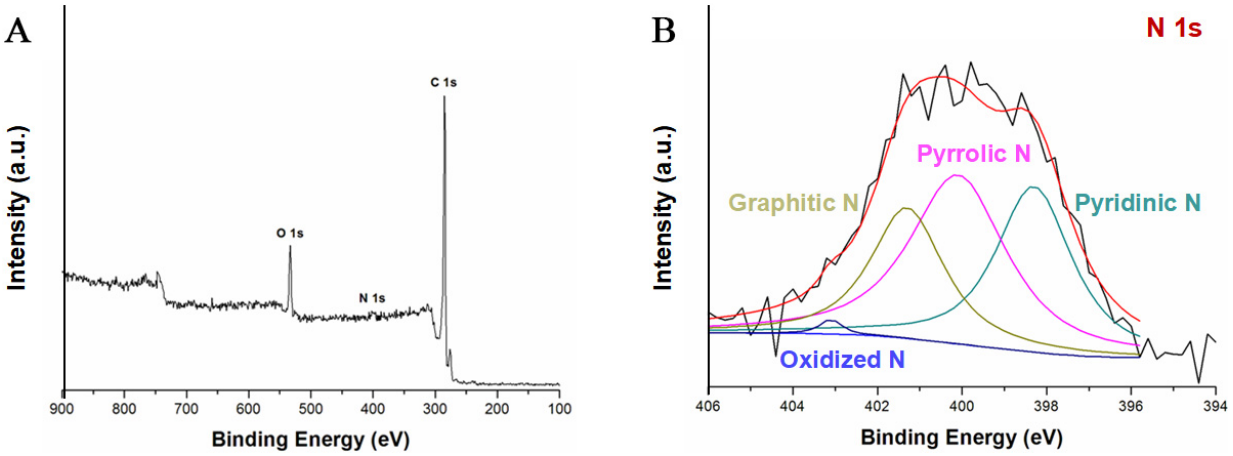

Figure 7. (A) XPS survey spectrum of Fe_3O_4@C-N microspheres; (B) High-resolution N 1s spectrum and peak deconvolution of Fe_3O_4@C-N: the black curve is the experimental data, the red curve is the overall fitted envelope, and the colored component peaks are assigned to pyridinic N (~ 398.3 eV), pyrrolic N (~ 400.0 eV), graphitic N (~ 401.3 eV), and oxidized N (~ 403.1 eV); the baseline/background used for fitting is also shown. XPS: X-ray photoelectron spectroscopy.

DECLARATIONS

Authors' contributions

Made substantial contributions to conception and design of the study and performed data analysis and interpretation, funding acquisition: Yue, Q.; Pan, P.

Performed data acquisition and provided administrative, technical, and material support: Shao, X.; Xing, Y.; Cheng, X.

Availability of data and materials

All experimental methods and key results are fully described in the manuscript to ensure reproducibility of the work. Any additional relevant information can be obtained from the corresponding authors upon reasonable request.

AI and AI-assisted tools statement

Not applicable.

Financial support and sponsorship

This work was financially supported by the National Natural Science Foundation of China (22409025 and 52571104), the National Key Research and Development Program of China (No. 2025YFE0212900), the Natural Science Foundation of Sichuan Province (2025NSFTD0003, 2025ZDZX0083), the Natural Science Foundation of Shandong Province (ZR2024MH104), the Interdisciplinary Cultivation Program at Shandong University, Weihai, and the Physical-Chemical Materials Analytical & Testing Center of Shandong University at Weihai.

Conflicts of interest

Yue, Q. is an Editorial Board Member of the journal *Micro Nano Science*. Yue, Q. was not involved in any steps of the editorial process, including reviewers' selection, manuscript handling, or decision-making. The other authors declare that there are no conflicts of interest.

Ethical approval and consent to participate

Not applicable.

Consent for publication

Not applicable.

Copyright

Supplementary Materials

Supplementary Materials

REFERENCES

1. Hu, F.; Hu, Z.; Liu, Y.; et al. Aqueous sol-gel synthesis and shaping of covalent organic frameworks. *J. Am. Chem. Soc.* **2023**, *145*, 27718-27. DOI PubMed
2. Tian, Y.; Chen, Y.; Wang, S.; et al. Ultrathin aerogel-structured micro/nanofiber metafabric via dual air-gelation synthesis for self-sustainable heating. *Nat. Commun.* **2024**, *15*, 6416. DOI PubMed PMC
3. Hermans, T. M.; Singh, N. Chemically fueled autonomous Sol → Gel → Sol → Gel → Sol transitions. *Angew. Chem.* **2023**, *135*, e202301529. DOI PubMed
4. Lim, H. W.; Lee, T. K.; Park, S.; et al. A ruthenium-titania core-shell nanocluster catalyst for efficient and durable alkaline hydrogen evolution. *Energy Environ. Sci.* **2025**, *18*, 2243-53. DOI
5. Xie, W.; Huang, X. Y.; Zhu, C.; et al. Synthesis of ordered mesoporous metal oxides by solvent evaporation-induced cooperative assembly. *Nat. Protoc.* **2026**, *21*, 987-1020. DOI PubMed
6. Li, J.; Liu, S.; Xie, Y.; et al. Nanoemulsion-assisted assembly and polymerization towards core-shell magnetic mesoporous melamine-formaldehyde resin microspheres. *Chin. Chem. Lett.* **2026**, *37*, 111433. DOI
7. Xie, Y.; Xie, W.; Li, J.; Deng, Y.; Cheng, X. Ternary interactions balance enabled sequential assembly toward the synthesis of hierarchically mesoporous metal hydroxide nanoparticles. *J. Am. Chem. Soc.* **2025**, *147*, 28882-92. DOI PubMed
8. Tong, T.; Hu, H.; Xie, Y.; Jin, J. Advancements in liquid marbles as an open microfluidic platform: Rapid formation, robust manipulation, and revolutionary applications. *Droplet* **2025**, *4*, e160. DOI
9. Xing, E.; Yu, Y.; Yu, H.; et al. Solvation-layer mediated interfacial assembly for surface topological engineering of mesoporous microcarriers. *ACS Nano* **2025**, *19*, 33798-812. DOI PubMed
10. Millot, Y.; Hervier, A.; Ayari, J.; Hmili, N.; Blanchard, J.; Boujday, S. Revisiting alkoxysilane assembly on silica surfaces: grafting versus homo-condensation in solution. *J. Am. Chem. Soc.* **2023**, *145*, 6671-81. DOI PubMed
11. Wolf, A.; Sauer, J.; Hurle, K.; Müssig, S.; Mandel, K. Magnetic supraparticles capable of recording high-temperature events. *Adv. Funct. Mater.* **2024**, *34*, 2316212. DOI
12. Chen, J.; Hua, Z.; Yan, Y.; Zakhidov, A. A.; Baughman, R. H.; Xu, L. Template synthesis of ordered arrays of mesoporous titania spheres. *Chem. Commun. (Camb).* **2010**, *46*, 1872-4. DOI PubMed
13. Xie, W.; Huang, X.; Zhu, C.; et al. A versatile synthesis platform based on polymer cubosomes for a library of highly ordered nanoporous metal oxides particles. *Adv. Mater.* **2024**, *36*, e2313920. DOI PubMed
14. Kuang, J.; Wang, Q.; Jia, Z.; et al. Ablation-resistant yttrium-modified high-entropy refractory metal silicide (NbMoTaW)Si_2 coating for oxidizing environments up to 2,100 °C. *Mater. Today* **2024**, *80*, 156-66. DOI
15. Ren, Z.; Wang, M.; Chen, S.; et al. Suppressing the formation of OP4 phase in P2-Structured $Na_{0.67}N_{i0.1}Co_{0.1}Mn_{0.8}O_2$ by *in-situ* formed NiF_2 layer. *Energy Storage Mater.* **2023**, *60*, 102815. DOI
16. Pan, P.; Liu, Q.; Hu, L.; et al. Dual-template induced interfacial assembly of yolk-shell magnetic mesoporous polydopamine vesicles with tunable cavity for enhanced photothermal antibacterial. *Chem. Eng. J.* **2023**, *472*, 144972. DOI
17. Xie, W.; Ren, Y.; Jiang, F.; et al. Solvent-pair surfactants enabled assembly of clusters and copolymers towards programmed mesoporous metal oxides. *Nat. Commun.* **2023**, *14*, 8493. DOI PubMed PMC
18. Quan, Q.; Fan, C.; Pan, N.; et al. Tough and stretchable phenolic-reinforced double network deep eutectic solvent gels for multifunctional sensors with environmental adaptability. *Adv. Funct. Mater.* **2023**, *33*, 2303381. DOI
19. Li, K.; Ni, X.; Li, D.; et al. Efficient construction of low shrinkage xerogels via coordination-catalyzed *in-situ* polymerization for activated carbon xerogels with multi-dyes adsorption. *Nano Materials Science* **2025**, *7*, 674-85. DOI
20. Al-Muhtaseb, S.; Ritter, J. Preparation and properties of resorcinol-formaldehyde organic and carbon gels. *Adv. Mater.* **2003**, *15*, 101-14. DOI
21. Zhou, X.; Ma, J.; Ren, Y.; Zou, Y.; Zhao, D.; Deng, Y. Bridging molecule assisted organic-inorganic interface coassembly to rationally construct metal oxide mesostructures. *Chem. Mater.* **2022**, *34*, 6824-34. DOI
22. Feng, B.; Wu, Y.; Ren, Y.; et al. Self-template synthesis of mesoporous Au-SnO_2 nanospheres for low-temperature detection of triethylamine vapor. *Sensor Actuat. B-Chem.* **2022**, *356*, 131358. DOI
23. Ren, Y.; Xie, W.; Li, Y.; et al. Noble metal nanoparticles decorated metal oxide semiconducting nanowire arrays interwoven into 3D mesoporous superstructures for low-temperature gas sensing. *ACS Cent. Sci.* **2021**, *7*, 1885-97. DOI PubMed PMC

24. Luo, Y.; Wang, X.; Wang, P.; Chen, F.; Yu, H. Inorganic/organic hybrid interfacial internal electric field modulated charge separation of resorcinol-formaldehyde resin for boosting photocatalytic H_2O_2 production. *Chem. Eng. J.* **2024**, *497*, 154886. DOI
25. Shiraishi, Y.; Matsumoto, M.; Ichikawa, S.; Tanaka, S.; Hirai, T. Polythiophene-doped resorcinol-formaldehyde resin photocatalysts for solar-to-hydrogen peroxide energy conversion. *J. Am. Chem. Soc.* **2021**, *143*, 12590-9. DOI PubMed
26. Itoh, Y.; Fu, T.; Champagne, P. L.; et al. Electric double-layer synthesis of a spongelike, lightweight reticular membrane. *Science* **2025**, *389*, 73-7. DOI PubMed
27. Yu, X. Q.; Wu, J.; Wang, J. W.; et al. Facile access to high solid content monodispersed microspheres via dual-component surfactants regulation toward high-performance colloidal photonic crystals. *Adv. Mater.* **2024**, *36*, e2312879. DOI PubMed
28. Parker, C. J.; Krishnamurthi, V.; Zuraiqi, K.; et al. Synthesis of planet-like liquid metal nanodroplets with promising properties for catalysis. *Adv. Funct. Mater.* **2023**, *34*, 2304248. DOI
29. Jung, W.; Vong, M. H.; Kwon, K.; et al. Giant decrease in interfacial energy of liquid metals by native oxides. *Adv. Mater.* **2024**, *36*, e2406783. DOI PubMed PMC
30. Chen, Y.; Liu, L.; Li, J.; et al. Flexible gas sensors based on *in situ* fabricated hierarchically porous SnO_2/PEDOT:PSS sensing layer. *Chin. Chem. Lett.* **2026**, *37*, 111654. DOI
31. Wang, F.; Zhong, H.; Chen, Z.; et al. Porous 2D CuO nanosheets for efficient triethylamine detection at low temperature. *Chin. Chem. Lett.* **2023**, *34*, 107392. DOI
32. Wang, X.; Zhou, J.; Xing, W.; et al. Resorcinol-formaldehyde resin-based porous carbon spheres with high CO2 capture capacities. *J. Energy Chem.* **2017**, *26*, 1007-13. DOI
33. Zhang, Z.; Liu, M.; Ibrahim, M. M.; et al. Flexible polystyrene/graphene composites with epsilon-near-zero properties. *Adv. Compos. Hybrid Mater.* **2022**, *5*, 1054-66. DOI
34. Li, H. J.; Chen, Y.; Wang, H.; et al. Amide (n, π*) Transitions enabled clusteroluminescence in solid-state carbon dots. *Adv. Funct. Mater.* **2023**, *33*, 2302862. DOI
35. Xiao, P.; Zhang, Z.; Ge, J.; et al. Surface passivation of intensely luminescent all-inorganic nanocrystals and their direct optical patterning. *Nat. Commun.* **2023**, *14*, 49. DOI PubMed PMC
36. Lan, Y.; Zheng, G. S.; Song, R. W.; et al. Low-temperature molten-salt enabled synthesis of highly-efficient solid-state emitting carbon dots optimized using machine learning. *Nat. Commun.* **2025**, *16*, 8167. DOI PubMed PMC
37. Deng, S.; Locklin, J.; Patton, D.; Baba, A.; Advincula, R. C. Thiophene dendron jacketed poly(amidoamine) dendrimers: nanoparticle synthesis and adsorption on graphite. *J. Am. Chem. Soc.* **2005**, *127*, 1744-51. DOI PubMed
38. Guo, Z. M.; Gao, Y. X.; Lin, T. Synthesis of nanosized tungsten carbide from phenol formaldehyde resin coated precursors. *Rare Metals* **2008**, *27*, 201-4. DOI
39. Wang, X.; Liao, Y.; Zhang, D.; Wen, T.; Zhong, Z. A review of Fe_3O_4 thin films: synthesis, modification and applications. *J. Mater. Sci. Technol.* **2018**, *34*, 1259-72. DOI
40. Xu, Q.; Qu, H.; Wu, Z.; et al. Relaxation-enhanced polymer nanocomposites induced by bound polymer loops on the particle surfaces. *Nat. Commun.* **2025**, *16*, 9870. DOI PubMed PMC
41. Paris, J. L.; Gaspar, R.; Coelho, F.; De Beule, P. A. A.; Silva, B. F. B. Stability criterion for the assembly of core-shell lipid-polymer-nucleic acid nanoparticles. *ACS Nano* **2023**, *17*, 17587-94. DOI PubMed PMC
42. Lee, D.; Wolska-Pietkiewicz, M.; Badoni, S.; Grala, A.; Lewiński, J.; De Paëpe, G. Disclosing interfaces of ZnO nanocrystals using dynamic nuclear polarization: sol-gel versus organometallic approach. *Angew. Chem. Int. Ed. Engl.* **2019**, *58*, 17163-8. DOI
43. Fijneman, A. J.; Högblom, J.; Palmlöf, M.; De With, G.; Persson, M.; Friedrich, H. Multiscale colloidal assembly of silica nanoparticles into microspheres with tunable mesopores. *Adv. Funct. Mater.* **2020**, *30*, 2002725. DOI PubMed PMC
44. Siegwardt, L.; Gallei, M. Complex 3D-Printed Mechanochromic Materials with iridescent structural colors based on core-shell particles. *Adv. Funct. Mater.* **2023**, *33*, 2213099. DOI
45. Lin, C.; Li, Y.; Yu, M.; Yang, P.; Lin, J. A facile synthesis and characterization of monodisperse spherical pigment particles with a core/shell structure. *Adv. Funct. Mater.* **2007**, *17*, 1459-65. DOI
46. Chen, Z.; Chu, C.; Yao, D.; Li, Q.; Mao, S. Resorcinol-phthalaldehyde resins for photosynthesis of hydrogen peroxide: modulation of electronic structure and integration of dual channel pathway. *Adv. Funct. Mater.* **2024**, *34*, 2400506. DOI
47. Li, J.; Liu, S.; Xie, Y.; et al. Core-shell magnetic mesoporous 3-aminophenol-formaldehyde resin microspheres with rich functional groups via interface co-assembly and polymerization. *J. Mater. Chem. A.* **2024**, *12*, 22627-36. DOI
48. Zou, Y.; Sun, Z.; Wang, Q.; et al. Core-shell magnetic particles: tailored synthesis and applications. *Chem. Rev.* **2025**, *125*, 972-1048. DOI
49. Sui, C.; Hsu, P. Standardizing the thermodynamic definition of daytime subambient radiative cooling. *ACS Energy Lett.* **2024**, *9*, 2997-3000. DOI

50. Xu, H.; Wang, N.; Meng, R.; et al. Rapid grain growth to attain over 13% certified flexible CZTSSe solar cell. *ACS Energy Lett.* **2025**, *10*, 4644-54. DOI
51. Qu, X.; Chu, F.; He, Y.; et al. Atomic-scale structural dynamics at a-Si:H/c-Si heterointerface during low-temperature thermal annealing. *Adv. Funct. Mater.* **2024**, *35*, 2413141. DOI
52. Moreira, M.; Pires, A. L.; Ferreira-Teixeira, S.; et al. Promoting surface conduction through scalable structure engineering of flexible topological insulator thin films. *Adv. Funct. Mater.* **2024**, *34*, 2405057. DOI
53. Zhao, Q.; Tang, R.; Che, B.; et al. Grain-boundary elimination via liquid medium annealing toward high-efficiency Sb_2Se_3 solar cells. *Adv. Mater.* **2025**, *37*, e2414082. DOI
54. Chai, Z.; Peng, B.; Ren, X.; Hong, K.; Chen, X. The microstructural evolution and relaxation strengthening for nano-grained Ni upon low-temperature annealing. *Nano Mater. Sci.* **2024**, *6*, 726-34. DOI
55. Gholami, F.; Yue, L.; Li, M.; et al. Fast and Efficient fabrication of functional electronic devices through grayscale digital light processing 3D printing. *Adv. Mater.* **2024**, *36*, e2408774. DOI
56. Qian, Z.; Zhao, S.; Li, B.; Wu, G. P. Dual sacrificial strategy toward tough and recyclable CO_2-sourced epoxy thermosets. *Angew. Chem. Int. Ed. Engl.* **2025**, *64*, e19660. DOI
57. Yue, L.; Su, Y. L.; Li, M.; et al. Chemical circularity in 3D printing with biobased Δ-valerolactone. *Adv. Mater.* **2024**, *36*, e2310040. DOI
58. Lee, Y. B.; Kim, Y. S.; Chen, C.; et al. Multimaterial 3D printing in activating bath enables *in situ* polymerization of thermosets with intricate geometries and diverse elastic behaviors. *Adv. Mater.* **2025**, *37*, e08568. DOI
59. Li, Q.; Cai, S.; Feng, Z.; et al. Chemically recyclable carbon fiber reinforced polymer composites with ultrafast degradation rate via an epoxy monomer bearing four acetal groups. *Adv. Funct. Mater.* **2025**, *36*, e24492. DOI
60. Yu, L.; Pan, P.; Yu, B.; et al. Interface assembly to magnetic mesoporous organosilica microspheres with tunable surface roughness as advanced catalyst carriers and adsorbents. *ACS Appl. Mater. Interfaces* **2021**, *13*, 36138-46. DOI